International Journal of Advanced Engineering and Management Research

Vol. 10, No. 04; 2025

ISSN: 2456-3676

Development of an Automatic Region of Interest Extraction Model for Lung Cancer Candidates in CT Scan Images

Sri Widodo[1*], Mohammad Faizuddin Bin MD Noor[2], Zalizah Awang Long[3]

[1]Health Science Faculty, Universitas Duta Bangsa Surakarta, Central Java, Indonesia
Jalan K.H. Samanhudi 93, Surakarta, 57147, Central Java, Indonesia

[2]Unikl Malaysian Institute of Information Technology, Universiti Kuala Lumpur, Malaysia
Jalan Sultan Ismail, 50250 Kuala Lumpur Malaysia

[3]Unikl Malaysian Institute of Information Technology, Universiti Kuala Lumpur, Malaysia
Jalan Sultan Ismail, 50250 Kuala Lumpur Malaysia

doi.org/10.51505/ijaemr.2025.1308 URL: http://dx.doi.org/10.51505/ijaemr.2025.1308

Received: July 21, 2025 Accepted: July 29, 2025 Online Published: Aug 20, 2025

Abstract

Lung cancer is the uncontrolled proliferation of cancer cells in lung tissue. Recently, numerous researchers have started working on lung cancer detection. The technique for detecting lung cancer begins with selecting the Region of Interest (ROI). ROI extraction in lung cancer diagnosis requires two steps: lung field segmentation and cancer candidate segmentation. Earlier research on lung cancer detection used manual ROI extraction, generally through cropping. Automatic segmentation can be hard, especially when separating the lung field from adjacent tissues. If the anomaly is significant and located near the lung's edge, the lung's edge may become obscured. When segmentation is conducted, the image suspected of being cancerous is excluded from the lung image (the diseased portion of the lung is gone). Thus, lung field segmentation is regarded to have failed. The suggested study intends to create a Region of Interest (ROI) extraction algorithm for automatic cancer candidate segmentation on CT scan images utilising the Active Shape algorithm and mathematical morphology techniques. The proposed research is separated into two stages: lung field segmentation using the Active Shape Model (ASM), and lung candidate segmentation using the mathematical morphology method. The Active Shape Model technique achieves 97.28% lung segmentation accuracy, with 96% sensitivity and 97.4% specificity. Meanwhile, the Morphology technique achieves 99.4% accuracy in lung cancer candidate segmentation, with 96.2% sensitivity and 99.7% specificity.

Keywords: ASM, CNN, Morphology, ROI.

1. Introduction

In general, lung cancer refers to all forms of cancer in the lungs, including cancer that develops within the lungs and cancer that develops outside the lungs (tumour metastasis in the lungs) (American Lung Association, 2023) (Widodo et al., 2020). Nodules are small, round, or egg-shaped lesions in the lungs that are considered benign tumours. The diameter of pulmonary

Vol. 10, No. 04; 2025

ISSN: 2456-3676

nodules or benign tumours is usually 3-4 cm (no more than 6 cm) and they are always surrounded by healthy lung tissue. (Halmos et al., 2019) (Thompson et al., 2019) (Kustanto, Widodo & Tomo, 2015) (Zhou et al., 2016) (Abbas, 2017) (Tian et al., 2012) (Song et al., 2017) (Tran et al., 2019). Lung cancer can usually be identified visually by a doctor using CT scan images. The diagnostic procedure involves reviewing a set of 2-D CT scan images and evaluating each scan individually. The printed results are read by projecting the CT and X-ray images onto a lightbox. This method is, of course, less effective. The diagnosis of lung cancer, whether benign or malignant, can vary depending on the pulmonologist (Makaju et al., 2018). It may also depend on the kind, shape, size, and location of the cancer in the lung organ (Colakoglu et al., 2019). Early identification of lung cancer using CT scan pictures is critical.

Recently, many researchers have applied artificial intelligence (AI) to detect lung cancer. The first study was conducted by Atsushi (Teramoto et al., 2019). The study used a deep convolutional neural network (CNN) to automatically categorise cancerous lung cells from microscopic pictures. The images were captured using a digital camera mounted on an optical lens with a 40mm focal length. Region of interest (ROI) extraction was performed manually via cropping. Data augmentation was employed to generate images through rotation, flipping, filtering, and colour adjustment. Based on the VGG-16 model adapted with Afine, the DCNN categorisation was completed. The malignant cancer image area was segmented with patches, and classification accuracy was assessed using three-fold cross-validation. The classification findings showed that the sensitivity and specificity were 89.3% and 83.3%, respectively.

The next study is from Yuya Onishi (Onishi et al., 2019). The study used a deep convolutional neural network (DCNN) to automatically classify lung nodules on CT data. ROI extraction was achieved through hand cropping. The purpose of this study was to see if utilising generative adversarial networks (GANs) to produce a huge number of images will increase classification accuracy. The proposed technique was used to analyse CT scans from 60 cases with pathologically verified diagnoses via biopsy. Using this pretraining and fine-tuning procedure, 66.7% of benign nodules could be distinguished from 93.9% of malignant nodules. These results show that the proposed strategy enhances classification success by about 20% compared to training with only original photos.

A new deep learning technique was proposed by Giang Son Tran (Tran et al., 2019) to improve the accuracy of lung nodule detection classification. The objective of this study was to categorise potential lung lesions on CT scans as nodules or non-nodules. ROI extraction was performed by manual cropping. Automatic feature extraction and classification techniques used 15 layers. After training, the Focal Loss function was used to improve categorisation accuracy. The deep learning technique using focus loss resulted in high-quality classification with 97.3% accuracy, 96.0% sensitivity, and 97.2% specificity.

From the research conducted by several researchers above, ROI extraction was performed manually through cropping. ROI operations are critical in lung cancer detection. ROI extraction

Vol. 10, No. 04; 2025

ISSN: 2456-3676

in lung cancer diagnosis consists of two activities: lung field segmentation and lung cancer candidate segmentation. ROI operations are used to obtain objects to be detected, in this case images suspected of being lung cancer (cancer candidates). This procedure is tough, particularly segmenting the lung field, which entails isolating the lung portion from the surrounding tissue. If the abnormality is large and placed near the lung's edge, it can cause the lung's edge to become indistinct. This means that if segmentation is performed, the picture suspected of being malignant will be excluded from the lung image. Thus, lung segmentation is deemed unsuccessful. The proposed study attempts to create an automatic Region of Interest (ROI) extraction model on CT scan images utilising the Active Shape Model and mathematical morphology methodologies. The proposed study is divided into two stages: lung field segmentation with the Active Shape Model methodology and lung candidate segmentation using the Mathematical Morphology method. This study aims to improve the accuracy of detecting lung cancer in CT scan images.

2. Method

2.1. Materials

2.1.1. Data Source

Data were gathered from the LIDC-IDRI (Lung Image Database Consortium Image Collection), National Biomedical Imaging Archive (NBIA) a public dataset widely used for lung cancer detection research, and hospitals.

2.1.2. Data Format and Size

a. File Format: DICOM (.dcm)
b. Dataset Size: Approximately 4 GB
c. Number of Patients: ±100 patients
d. Number of Images per Patient: Varies, between 60 and 100 slices.

2.1.3. Image Resolution and Size

a. Standard Resolution: 512 x 512 pixels
b. Slice Thickness: Ranges from 0.6 mm to 5.0 mm
c. Spatial Resolution: Depends on the CT device used; typically 0.5-0.8 mm per pixel.

2.1.4. Colour and Intensity Scale

a. Colour Type: Grayscale (8-bit or 16-bit grayscale)
b. Intensity Range: -1,000 to +3,000 Hounsfield Units (HU), but usually converted to the [0, 255] range for preprocessing and model training purposes.

Vol. 10, No. 04; 2025

ISSN: 2456-3676

2.2. ROI Extraction Process

Region of Interest (ROI) extraction was performed by segmenting CT images to obtain images suspected of being lung cancer. The proposed ROI extraction model is shown in Figure 1.

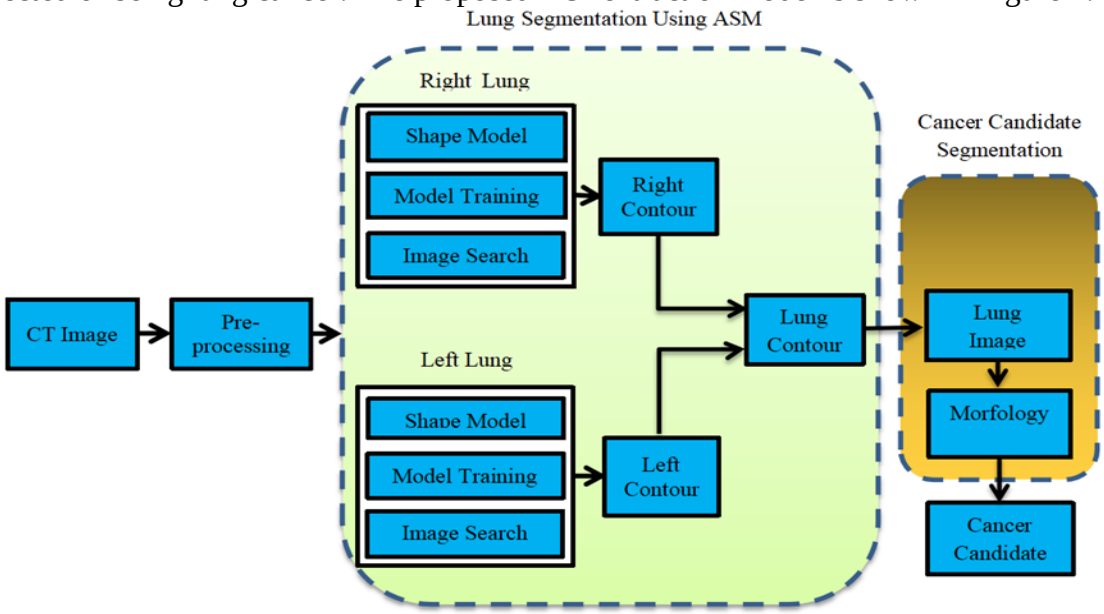

Figure 1. Proposed Modelling for ROI Extraction

The ROI extraction process consists of two stages. It can be explained in detail as follows.

2.2.1. Lung Field Segmentation

The first step in Region of Interest (ROI) extraction is lung image segmentation. The Active Shape Model (ASM) is the proposed approach for segmenting the lungs. Tim Cootes developed the Active Shape Model (ASM), a statistical model, in the 1990s (Cootes et al., 1995). The initial stage in ASM is to generate a model with landmark positions from the image in the training data. The steps in lung segmentation using ASM can be explained as follows.

1. Analysis Procrustes

a. Procrustes analysis is a statistical shape analysis methodology that operates on a set of shapes. In this case, the shapes are equal by altering the translation, rotation, and scale components. A brief description of the steps for matching shapes $X = (x_1, y_1, x_2, y_2, \ldots, x_n, y_n)$ and $Z = (z_1, w_1, z_2, w_2, \ldots, z_n, w_n)$ can be explained as follows:

b. Translation

Calculate the centre of mass for each shape:

$$\bar{x} = \frac{x_1 + \ldots + x_n}{n}, \bar{y} = \frac{y_1 + \ldots + y_n}{n}, \bar{z} = \frac{z_1 + \ldots + z_n}{n}, \bar{w} = \frac{w_1 + \ldots + w_n}{n} \quad (1)$$

Translate each shape to its centre of mass:

$$(x', y') \mapsto (x - \bar{x}, y - \bar{y}), (z', w') \mapsto (z - \bar{z}, w - \bar{w}) \quad (2)$$

c. Scaling

Calculate scaling for each shape using L2-norm:

$$ScaleX = \sqrt{x_1'^2 + y_1'^2 + x_2'^2 + y_2'^2 + \ldots + x_n'^2 + y_n'^2}$$

$$ScaleZ = \sqrt{z_1'^2 + w_1'^2 + z_2'^2 + w_2'^2 + \ldots + z_n'^2 + w_n'^2} \quad (3)$$

$$X' = \frac{X'}{ScaleX}, Z' = \frac{Z'}{ScaleZ} \quad (4)$$

d. Rotation

Construct $\underline{X}$ and $\underline{Z}$ as follows:

$$\underline{X} = \begin{pmatrix} x_1' & x_2' & \ldots & x_n' \\ y_1' & y_2' & \ldots & y_n' \end{pmatrix}, \underline{Z} = \begin{pmatrix} z_1' & z_2' & \ldots & z_n' \\ w_1' & w_2' & \ldots & w_n' \end{pmatrix} \quad (5)$$

Calculate Singular Value Decomposition (SVD) for $\underline{Z}^T * \underline{X}$ and find U, S, V. The rotation matrix (R) to match $\underline{Z}$ to $\underline{X}$:

$$R = V * U^T = \begin{pmatrix} \cos(\theta) & -\sin(\theta) \\ \sin(\theta) & \cos(\theta) \end{pmatrix} \quad (6)$$

Calculate

$$Z_{rotasi} = R * \underline{Z}. \quad (7)$$

2. Shape Alignment

The shapes of the elements in the training set differ in scale, rotation, and translation. These variations must be eliminated in order to obtain a stable form model. The traditional technique is to align all forms to the mean shape and repeat the process until the mean shape does not change in two consecutive iterations.

3. Principal Component Analysis (PCA)

PCA is a linear orthogonal transformation that maps a data set to a new coordinate system. The first dimension receives the data with the largest variation. The principal components are the eigenvectors of the covariance matrix. If $\sum_s$ is the covariance matrix of the training shapes, we have $\sum_s * P_s = P_s * \Lambda_s$ where Λ_s denotes a diagonal matrix of eigenvalues:

$$\Lambda_s = \begin{pmatrix} \lambda_{s,1} & \ldots & 0 \\ \vdots & \ddots & \vdots \\ 0 & \ldots & \lambda_{s,2N_t} \end{pmatrix} \quad (8)$$

Vol. 10, No. 04; 2025

ISSN: 2456-3676

4. Image Search

During this stage, an unseen image is used to manually estimate the shape. The first form should strike the object edges in the unseen image while remaining sensible. ASM then determines the best movement by examining the edge profile and covariance matrix of the mean normalised derivatives acquired in the previous stage.

5. The Initial Shape Estimation

First, the user should choose a shape as the starting shape. This form should be as close as possible to the target object in the image. If X_i is the original shape, it can be thought of as the translation, rotation, and scaling of a reference shape (X_{ref}).

$$X_i = M(s_i, \theta_i)[X_{ref}] + t_i \quad (9)$$

Were

$$M(s,\theta) = s \times \begin{pmatrix} \cos(\theta) & -\sin(\theta) \\ \sin(\theta) & \cos(\theta) \end{pmatrix} \quad (10)$$

$$t_i = [t_{x,i}, t_{y,i}, t_{x,i}, t_{y,i}, \ldots, t_{x,i}, t_{y,i}]^T \quad (11)$$

and X_{ref} is a combination of $\overline{X}$ and the model parameters:

$$X_{ref} = \overline{X} + P.b_{ref} \quad (12)$$

So, the final formulation is:

$$X_i = M(s_i, \theta_i)[\overline{X} + P.b_{ref}] + t_i \quad (13)$$

(Generally, $b_{ref} = 0$ so $X_{ref} = \overline{X}$)

6. Changes to the Pose and Model Parameters

To achieve satisfactory results, modify the basic shape by adjusting the pose and model parameters. These changes can be modelled as $X_i \to X_i + d_X$, means X_i is replaced by $X_i + d_X$, where $d_{X_i} = (d_{X_i pose}, d_{X_i \mathrm{mod}el})$, $d_{X_i pose} = (1 + d_s, d_\theta, d_t)$ and $d_{X_i \mathrm{mod}el} = P^T.d_b$. (14)

a. Calculate Pose Parameter Changes

The effects of posture parameter changes on the X_i are:

$$X_i = M(s_i, \theta_i)[X_{ref}] + t_i \xrightarrow{(1+d_s, d_\theta, d_t)} X_i + d_{X_i pose} \text{ or} \quad (15)$$

$$X_{temp} \Leftarrow M(s_i(1+d_s), \theta_i + d_\theta)[X_{ref}] + t_i + d_{t_i} \quad (16)$$

b. Calculate model parameter changes.

Vol. 10, No. 04; 2025

ISSN: 2456-3676

After adjusting the pose parameters, the remaining changes can be accomplished by tweaking the model parameters. These alterations only affect Xref in the final equations:

$$X_{ref} \to X_{ref} + d_{X_i \text{model}} \quad \text{atau} \quad X_{ref} \to X_{ref} + P^T d_b \tag{17}$$

So, the final X_i oleh d_{X_i} modification is:

$$X_i + d_{X_i} = M(s_i(1+d_s), \theta_i + d_\theta)[X_{ref} + d_{X_i \text{model}}] + t_i + d_{t_i} \tag{18}$$

By combination this equation with $X_i = M(s_i, \theta_i)[X_{ref}] + t_i$ and considering $M^{-1}(s,\theta) = M(s^{-1}, -\theta)$ we have:

$$d_{X_i \text{model}} = P^T . d_b = M((s_i(1+d_s))^{-1}, -\theta_i - d_\theta) \\ [M(s_i, \theta_i)X_{ref} + d_{X_i} - d_{t_i}] - X_{ref} \tag{19}$$

b. Calculate Each Landmark Movement

We know that the last equations are independent and have no relationship with the desired object in the unseen image. To enable this link, compute the edge profile for each landmark in the initial shape.

2.2.2. Lung Cancer Candidate Segmentation

The stages in candidate segmentation using morphological mathematics can be described as follows:

A. Image reduction for negative lung images. The reduction process has the following stages:

a. Lung images resulting from segmentation with ASM undergo a complement process, which will produce negative lung images. In binary images, the complement process transforms zeros into ones and vice versa. To obtain the complement of intensity or RGB images, subtract the maximum pixel value (255) from the value in the image. The complement of an image converts dark areas to light, and vice versa.

b. Deduct the lung image from the negative lung image.

c. The result of the above subtraction will undergo a morphological process.

B. Edge Detection

Edge detection is the technique of identifying substantial changes in an image's grey level. A image gradient measures differences in intensity level. For instance, if an image f(x,y) is a two-dimensional function, the gradient vectors of x and y are the first derivatives with respect to x and y, which may be written as an equation (Mark, 2008).

$$G = \begin{bmatrix} Gx \\ Gy \end{bmatrix} = \begin{bmatrix} \frac{\partial f(x,y)}{\partial x} \\ \frac{\partial f(x,y)}{\partial y} \end{bmatrix} \tag{20}$$

The gradient operator calculates changes in grey level intensity and direction of change. These changes are obtained from the value differences between neighbouring pixels. In two-dimensional images, gradients are approximated using equation 25.

$$G = \begin{bmatrix} Gx \\ Gy \end{bmatrix} = \begin{bmatrix} f(x+1,y) - (f(x,y) \\ f(x,y+1) - f(x,y) \end{bmatrix} \tag{21}$$

Vol. 10, No. 04; 2025

ISSN: 2456-3676

This equation can be stated in matrix form

G_x=[-1 1] (22)

Dan

$G_y=\begin{bmatrix} 1 \\ -1 \end{bmatrix}$ (23)

Meanwhile, the magnitude of the gradient can be computed using a variety of equation models, one of which is illustrated by equation 28.

$G[f(x,y)]=\sqrt{G_x^2+G_y^2}$ (24)

In this work, edge detection is performed utilising the Prewitt convolution approach. The Prewitt size is 3x3, with the horizontal element in the middle for Gx equal to 0 and the vertical element in the middle for Gy likewise equal to 0, as seen in equations 25 and 26 below.

$$G_x=\begin{bmatrix} 1 & 1 & 1 \\ 0 & 0 & 0 \\ -1 & -1 & -1 \end{bmatrix} \quad (25)$$

And

$$G_y=\begin{bmatrix} -1 & 0 & 1 \\ -1 & 0 & 1 \\ -1 & 0 & 1 \end{bmatrix} \quad (26)$$

C. Threshold

Thresholding is the technique of dividing pixels based on the degree of greyness. Pixels with a degree of greyness less than the specified threshold value are assigned the value 0, whereas pixels with a degree of greyness more than the threshold are assigned the value 1.

D. Dilatation

Dilatation adds pixels to the edges of each binary item, which are areas with a value of one. Dilatation creates 8 interconnected pixels around the item. Dilation is the process of combining background points (0) into a portion of the item (1). To employ dilation, position the centre point S at point A. Assign the value 1 to all points (x, y) that are affected or overlapped by structure S at that location. The dilation equation is illustrated in equation 27 below.

D(A,S)=A+S (27)

E. Filling the Image Area

To fill the image area, a morphological reconstruction approach is applied. The image area consists of dark pixels bordered by lighter pixels. After determining the image position, the following step is to fill the location (image area) with four background neighbour connections for 2-D input images and six background neighbour connections for 3-D input. This method produces areas surrounded by light-colored pixels with a value of one.

Vol. 10, No. 04; 2025

ISSN: 2456-3676

F. Erosion

Erosion removes 8 pixels from binary objects that are related to the object's edges. Erosion is the process of removing object points (1) and incorporating them into the background (0). To employ erosion, locate the pivot point S at point A. If any part of S is outside of A, the pivot point is eliminated or changed to background. Equation 28 illustrates erosion.

$$E(A,S)=AxS \quad (28)$$

G. Multiplication

Image multiplication is performed to obtain the final nodule candidate image. Image multiplication can be performed by multiplying each pixel by a certain value. Mathematically, this can be modelled using equation 29 below.

$$\forall f(x,y); Nf(x,y) = f(x,y) * Th \quad (29)$$

$$\forall Nf(x,y); if \;\; Nf(x,y) > 255 \;\; then \; Nf(x,y) = 255 \quad (30)$$

with

Th ≥ 1

F(x,y) is the original image, and Nf(x,y) is the image resulting from multiplying the intensity of the original image by the value of Th. In this study, the multiplication process involves multiplying the candidate cancer mask image resulting from the erosion process with the complement subtraction image.

3. Result

The first experiment involved segmenting a CT scan image of the lungs from the 29th slice with a substantial abnormality, as illustrated in Figures 2 and 3.

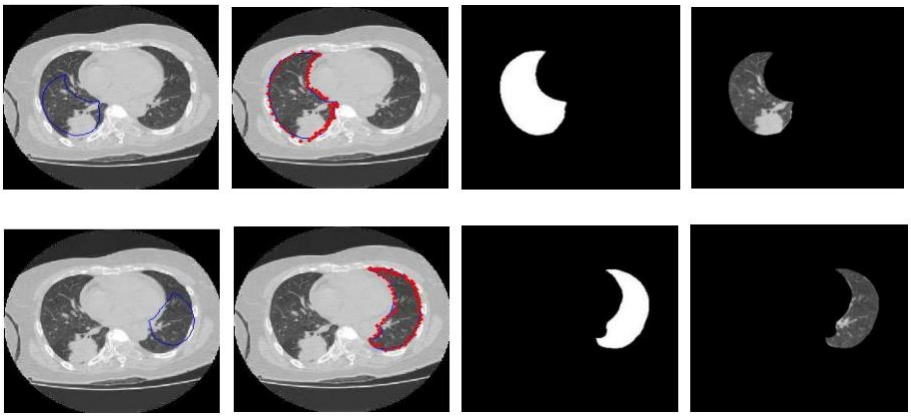

Figure 2. Segmentation Process with ASM

Figure 3 displays the findings of lung segmentation.

Vol. 10, No. 04; 2025

ISSN: 2456-3676

(a) (b)

Figure 3. (a) Lung Contour, (b). Final Lung Image

The complete lung segmentation results are given in Figures 4, 5, and 6.

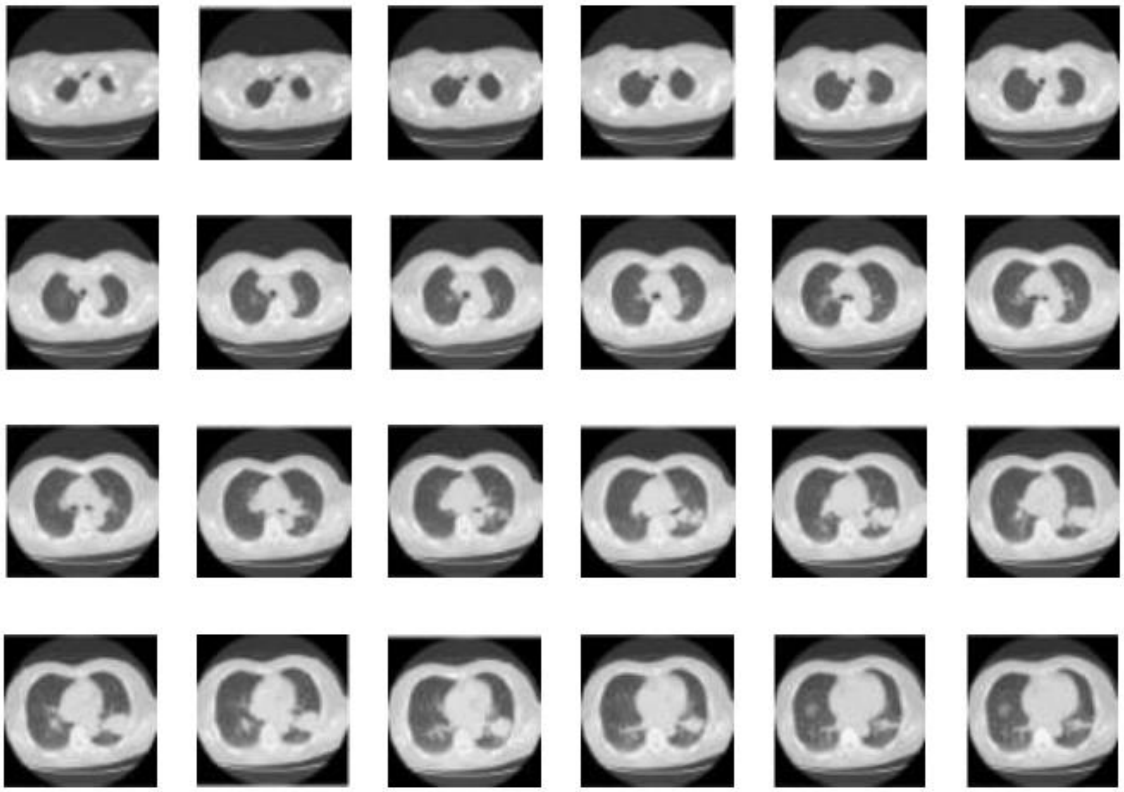

Figure 4. Sequential CT images of the patient

Vol. 10, No. 04; 2025

ISSN: 2456-3676

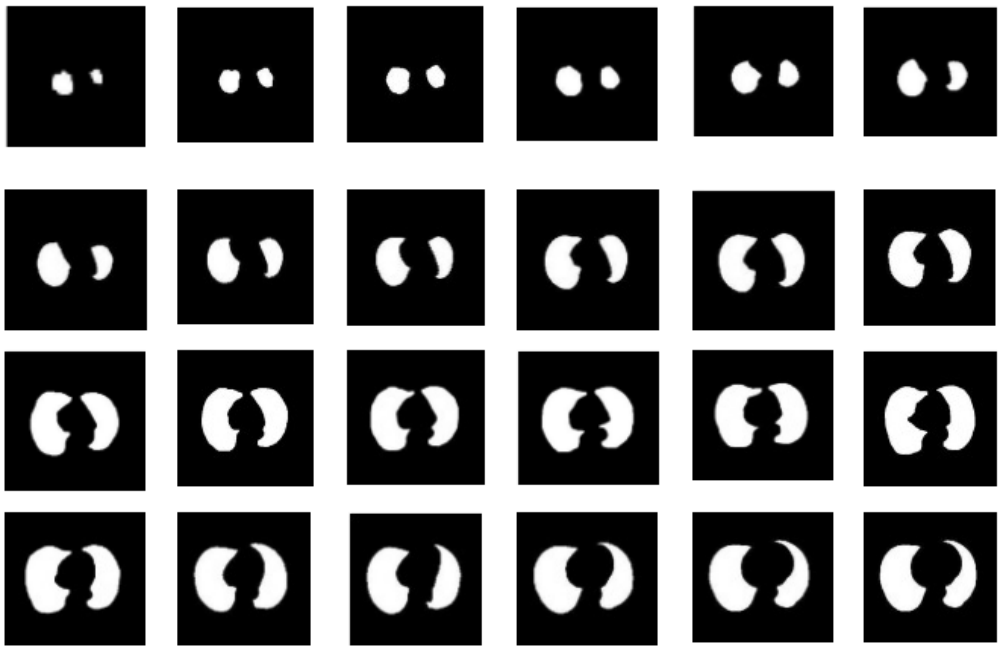

Figure 5. Contour of Segmentation Results with ASM

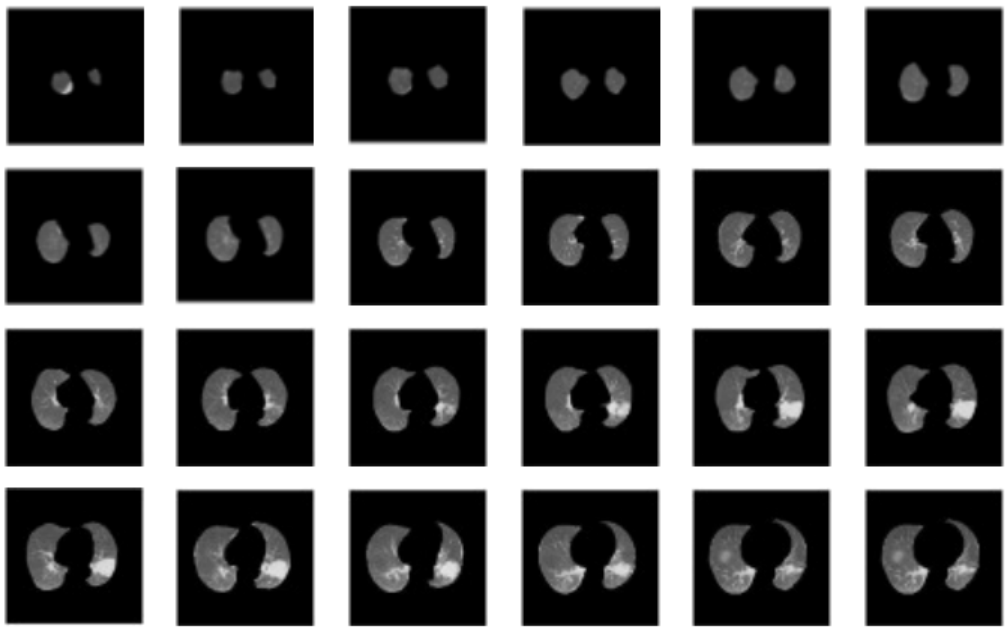

Figure 6. Image of the lungs

Figure 7 shows a comparison of segmentation results obtained using thresholding, active contour segmentation, and ASM. In the thresholding and active contour approaches, if the anomaly is large, it is not included in the lung picture.

Vol. 10, No. 04; 2025

ISSN: 2456-3676

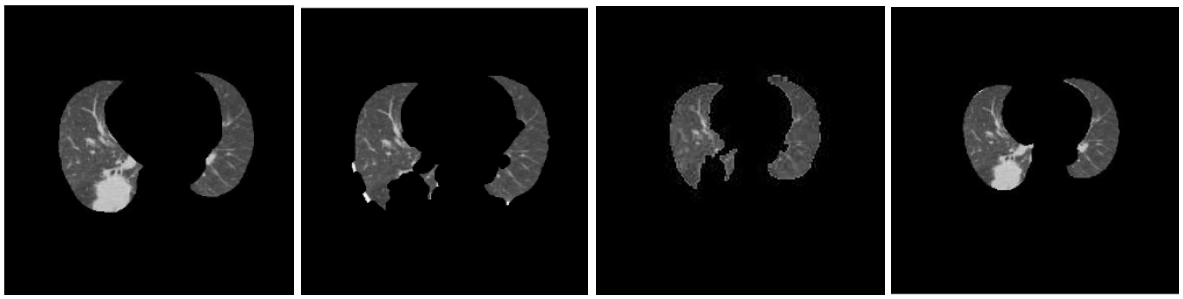

(a) (b) (c) (d)

Figure 7. Lung Segmentation Results in Great Shape abnormalities

(a) Manual segmentation Results by Groundthruth, (b). With Thresholding Segmentation, (c). The results of the Active Contour Segmentation, (d) Segmentation with ASM.

To determine the accuracy of the lung segmentation approach, the Active Shape Model (ASM) method was compared to ground truth lung segmentation data. The ground truth lung segmentation process is completed by outlining the lung borders on the original CT scan image with the Paint software. To calculate the accuracy, sensitivity, and specificity of lung segmentation, the segmentation data obtained by ASM is combined with the segmentation image obtained through ground truth. The observed pixels were then classified into four categories: TP (true positive), TN (true negative), FP (false positive), and FN (false negative). TP denotes lung pixels that were accurately identified as lung pixels. TN refers to non-lung pixels that have been accurately detected. FP refers to non-lung pixels that have been wrongly labelled as lung pixels. FN represents lung pixels that were not detected. To assess the performance of the suggested segmentation approach, accuracy, sensitivity, and specificity were determined. Accuracy represents the effectiveness of the given procedure. Sensitivity refers to the proportion of lung pixels that are accurately recognised. Meanwhile, specificity refers to the proportion of non-lung pixels that are not wrongly identified as lung. The formulas for accuracy, sensitivity, and specificity are as follows:

$$Akurasi = \frac{TP+TN}{TP+FP+FN+TN} \quad (31)$$

$$Sensitivitas = \frac{TP}{TP+FN} \quad (32)$$

$$Spesifisitas = \frac{TN}{TN+FP} \quad (33)$$

Table 1 shows the findings of ASM-based lung area segmentation.

Vol. 10, No. 04; 2025

ISSN: 2456-3676

Table 1. Results of Lung Segmentation Testing Using Active Shape Model

NO	IMAGES	TP	TN	FP	FN	ACCURACY %	SENSITIVITY %	SPECIFICITY %
1	0005-000040	21892	90453	1536	384	98,3	98,2	98,3
2	0007-000065	21185	91514	1277	487	98,4	97,7	98,6
3	0008-000024	23493	88616	1667	1471	97,2	94,1	98,1
4	0008-000027	24853	87309	1403	687	98,1	97,3	98,4
5	0011-000026	51388	60803	1515	2094	86,6	96	80
5	0017-000014	40160	71296	3417	805	96,3	98	95,4
6	0018-000003	12401	10028	642	593	98,9	95,4	99,3
7	0019-000012	22529	90086	1647	530	98,1	97,7	98,2
8	0023-000042	33789	77564	2658	1303	96,5	96,2	96,6
9	0023-000055	29811	81816	2004	691	97,6	97,7	97,6
10	0024-000010	22605	89659	1423	1928	97,1	92,1	98,4
11	0024-000013	20292	92038	1574	426	98,2	97,9	98,3
12	0024-000050	22570	89595	1751	1247	97,3	94,7	98
14	0030-000002	20019	92491	1246	445	98,5	97,8	98,6
15	0030-000013	29455	82493	1858	1380	97,1	95,5	97,7
16	0030-000014	30084	81912	2320	1225	96,9	96	97,2
17	0030-000015	29451	82594	2751	972	96,7	96,8	96,7
18	0032-000014	22165	90113	1899	884	97,5	96,11	97,9
19	0034-000044	24850	87148	2330	538	97,5	97,8	97,3
20	0035-000010	15016	97773	1171	372	98,6	97,5	98,8
21	0035-000017	16181	96116	972	297	98,8	98,1	98,9
22	0035-000018	17185	95171	1027	945	98,2	94,7	98,9
23	0035-000029	19769	92624	903	2061	97,4	90,5	99

Vol. 10, No. 04; 2025

ISSN: 2456-3676

24	0036-000014	27088	84672	2176	691	97,4	97,5	97,41
25	0036-000019	25637	86397	2951	2038	95,7	92,6	96,6
26	0036-000048	29226	82666	1085	3635	95,9	88,9	98,7
27	0037-000043	24149	87671	1244	1007	98	95,9	98,6
28	0040-000031	24236	88128	1122	717	98,3	97,1	98,7
29	0040-000032	26493	85593	1278	681	98,2	97,4	98,5
30	0040-000062	35093	76453	1667	1343	97,3	96,3	97,8
					Average	**97,2**	**96**	**97,4**

Table 2 shows the results of comparing the suggested method's accuracy to those of other approaches.

Table 2. Accuracy Comparison

Metode Segmentasi	Accuracy	Sensitivity	Specificity
Threshold	95.6	97.6	95.1
Active Contour	84.2	96.2	74.3
ASM	97.2	96	97.4

After segmenting the lung area, the second stage in determining the Region of Interest (ROI) is to use a morphological technique to segment images that are suspected of being lung cancer. Figure 8 depicts the results of the morphological method used to segment lung cancer candidates.

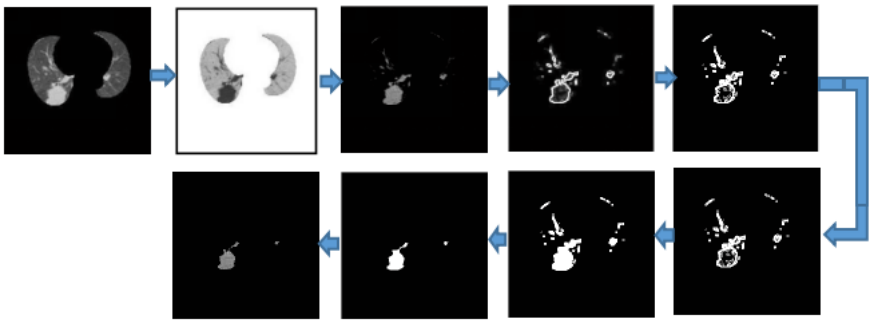

Figure 8 depicts the stages of the lung cancer candidate segmentation process.

To test the accuracy of the cancer candidate segmentation approach, segmentation results utilising the morphological method were compared to segmentation results obtained by ground truth. The lung cancer candidate segmentation process was conducted out by labelling photos

Vol. 10, No. 04; 2025

ISSN: 2456-3676

suspicious of abnormalities (nodules) with the Paint program. The cancer candidates' contours are obtained by segmenting the marked results using morphological mathematics. To calculate the accuracy, sensitivity, and specificity of lung organ segmentation, morphological mathematics segmentation results are combined with ground truth segmentation results, which are translated to unsigned integer (uint8) data type. The detected pixels are then divided into four categories: true positive (TP), true negative (TN), false positive (FP), and false negative (FN). TP is a lung cancer candidate pixel that was appropriately identified. TN is an accurately recognised non-lung cancer candidate pixel. FP is a non-lung cancer candidate pixel that has been classified as a lung cancer candidate pixel. Meanwhile, FN is a lung cancer candidate pixel that has not been discovered. To assess the performance of the suggested segmentation approach, accuracy, sensitivity, and specificity were determined. Accuracy represents the effectiveness of the given procedure. Sensitivity represents the proportion of lung pixels that are accurately recognised. Meanwhile, specificity refers to the proportion of pixels that are not lung cancer candidates and are not falsely identified as such. The results of the testing yielded accuracy, sensitivity, and specificity values as shown in Table 3.

Table 3. Results of Cancer Candidate Segmentation Testing

NO	IMAGES	TP	TN	FP	FN	ACCURACY %	SENSITIVITY %	SPECIFICITY %
1	PARU-09	1557	112671	6	96	99,9	94,1	99,9
2	PARU-10	3945	111507	432	126	99,5	96,9	99,6
3	PARU-11	5448	110799	432	255	99,4	95,5	99,6
4	PARU-12	8523	109612	6	384	99,6	95,6	99,9
5	PARU-13	11367	108212	678	288	99,1	97,5	99,9
6	PARU-14	12444	107940	621	453	99,1	96,4	99,4
7	PARU-15	13599	107502	711	858	98,7	94	99,3
8	PARU-16	11805	107956	27	171	99,8	98,5	99,9
9	PARU-17	9948	108839	9	72	99,9	99,2	99,9
10	PARU-18	7155	110132	15	441	99,6	94,1	99,9
		Average				**99,4**	**96,2**	**99,7**

The images of lung cancer and artery candidates extracted from ROI are shown in Figure 10.

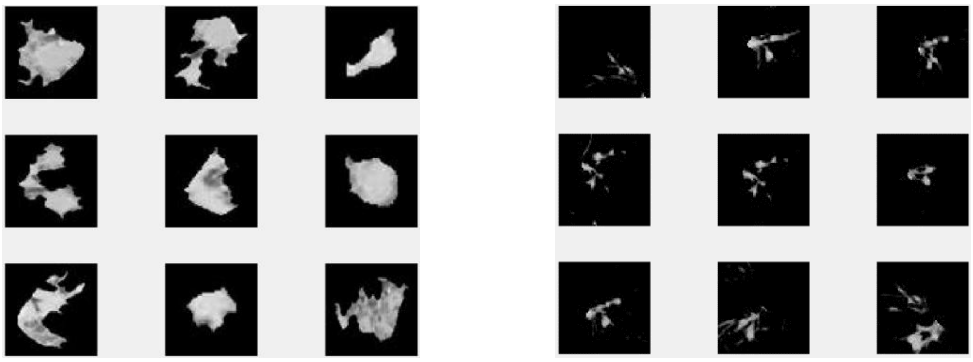

Figure 10. Images of Cancer Candidates and Arteries

Vol. 10, No. 04; 2025

ISSN: 2456-3676

4. Discussion

As previously stated, the automatic ROI extraction process comprises of two stages: lung area segmentation and lung cancer candidate segmentation. For lung area segmentation, three methods were tested: threshold, Active Contour Snake, and Active Shape Model (ASM). For lung cancer candidate segmentation, two methods were tested: Active Contour Snake and Morphological Mathematics. To assess the accuracy of the segmentation approaches, the Receiver Operating Characteristic (ROC) curve was utilised, which incorporates accuracy, sensitivity, and specificity. Accuracy was used as the primary evaluation parameter because it reflects the method's precision in identifying the entire lung area in medical images. The sensitivity value represents the method's ability to detect lung pixels as part of the relevant object. The specificity value reflects the segmentation method's ability to correctly identify non-lung areas. To determine the most suitable method, a statistical test was conducted. To find the best lung segmentation method, a Mann-Whitney statistical test was performed. This is because the data is not assumed to be normally distributed. For lung segmentation, compare the ASM method with the threshold, ASM with Active Contour Snake, and finally, the threshold with Active Contour Snake. Meanwhile, to find the best method for segmenting lung cancer candidates, a comparison test was conducted between the Active Contour Snake method and morphological mathematics. The results and discussion of the testing of lung segmentation models and lung cancer candidates are explained in detail as follows.

The first test was comparing the performance of the Active Shape Model (ASM) and the threshold technique. This test employs ROC operation data, which includes the accuracy, sensitivity, and specificity of each approach. A non-parametric Mann-Whitney U test was used to assess whether there is a significant difference in ROC accuracy between the Active Shape Model (ASM) and the threshold technique, as the data was not considered to be regularly distributed. The Mann-Whitney test on the accuracy data yielded the test statistic value U: 461.0 with a p-value of 0.00148. Because the p-value is smaller than the significance level of 0.05, it is possible to conclude that the two lung image segmentation methods differ statistically significantly in accuracy. This means that the difference in accuracy values produced by the two methods did not occur by chance. A descriptive examination of the accuracy figures reveals that the ASM approach has a mean of 97.27% with a standard deviation of 2.17%, whereas the threshold technique has a mean of 96.19% with a standard deviation of 1.54%. The greatest value obtained by the ASM approach is 98.92%, while the minimum value is 86.67%. Meanwhile, the threshold method achieves a maximum of 99.18% and a low of 93.66%. Although the threshold method produces the highest individual accuracy value, the ASM method demonstrates more stable and consistent performance in achieving high accuracy, as evidenced by its higher median value (97.54%) and third quartile (98.28%) compared to the threshold method. These results indicate that the ASM method consistently outperforms the threshold method in terms of lung image segmentation accuracy.

The following study will compare the performance of two lung image segmentation methods: the threshold technique and the active contour snake method. Based on descriptive statistics, the

Vol. 10, No. 04; 2025

ISSN: 2456-3676

ASM method has a higher average accuracy compared to the Active Contour Snake method, at 96.16% versus 92.81%. Additionally, the maximum accuracy value of ASM (99.17%) indicates the potential of this method to provide highly precise segmentation results. This statistically significant difference in accuracy indicates that the ASM method is superior in classifying lung and non-lung pixels overall. This advantage can be attributed to the characteristics of ASM, which integrates global and local shape information simultaneously.

The following study will compare the accuracy of two lung image segmentation methods: the threshold technique and the active contour snake method. The following study will compare the performance of two lung image segmentation algorithms, the threshold method and the active contour snake approach, using ROC metrics to determine accuracy, sensitivity, and specificity. Because the sample size is uneven and the data distribution is not considered to be normal, the Mann-Whitney U test is employed as a non-parametric statistical method to compare the two methods and decide whether there is a significant difference. The statistical test shows that the threshold technique has an average of 96.08%, while the active contour snake method has an average of 92.41%. Median accuracy: The threshold approach is more accurate than the Active Contour Snake method (96.32% vs. 92.45%). Additionally, the accuracy range of the threshold method is broader but still shows a high maximum value (up to 99.18%). From the Mann-Whitney test analysis, the results are U: 6.0, p-value: 0.007. Since the p-value is < 0.05, it can be concluded that there is a statistically significant difference between the accuracy of the threshold method and the active snake contour method. This means that the threshold method provides segmentation results with significantly better accuracy than the active snake contour method. Because the p-value is less than 0.05, we may conclude that there is a statistically significant difference in the accuracy of the threshold technique and the active snake contour method. This means that the threshold method provides segmentation results with significantly better accuracy than the active snake contour method.

For the segmentation of lung cancer candidates, two methods were tested. These methods are ASM-Morphology and ASM-Snake. To evaluate whether there were statistically significant differences, the Mann-Whitney test was applied to each method's accuracy statistics. Descriptive analysis revealed that the ASM-Morphology approach had an average accuracy of 99.5694% with a standard deviation of 0.3475, and the ASM-Snake method had an average accuracy of 82.9732% with a standard deviation of 3.2119. The Mann-Whitney test resulted in a U value of 0.0 and a p value of 0.00000022, which is significantly lower than the chosen significance level ($\alpha = 0.05$). These findings show a considerable difference in the accuracy of the ASM-Morphology and ASM-Snake approaches. The statistical test results show that the ASM-Morphology approach achieves much higher segmentation accuracy than the ASM-Snake method. The significant difference in average accuracy values, which reached approximately 16.6%, demonstrates the superiority of the ASM-Morphology method in detecting lung cancer candidates with greater accuracy and consistency. The smaller standard deviation in the ASM-morphology method also indicates that the segmentation results are more stable and less variable across experiments.

Vol. 10, No. 04; 2025

ISSN: 2456-3676

Conclusion

Based on the testing, the Region of Interest (ROI) extraction for lung region segmentation utilising the Active Shape Model technique has an accuracy of 97.2%, sensitivity of 96%, and specificity of 97.4%. The accuracy, sensitivity, and specificity of cancer candidate segmentation were 94.4%, 96.2%, and 99.7% respectively. This suggests that ROI extraction utilising the Active Shape Model and morphological approaches can serve as a model for automatic ROI extraction. This conclusion is based on the high accuracy, sensitivity, and specificity values.

Acknowledgment

We would like to thank Duta Bangsa University Surakarta for supporting my doctoral studies at Universiti Kuala Lumpur Malaysia.

References

Abbas, Q. (2017). Nodular-Deep: Classification of Pulmonary Nodules using Deep Neural Network. *International Journal of Medical Research & Health Sciences*, *6*(8), 111–118. www.ijmrhs.com

American Lung Association. (2023). *State of Lung Cancer*. https://www.lung.org/research/state-of-lung-cancer

Colakoglu, B., Alis, D., & Yergin, M. (2019). Diagnostic Value of Machine Learning-Based Quantitative Texture Analysis in Differentiating Benign and Malignant Thyroid Nodules. *Journal of Oncology*, *2019*. https://doi.org/10.1155/2019/6328329

Cootes, T. F., Taylor, C. J., Cooper, D. H., & Graham, J. (1995). COMPUTER VISION AND IMAGE UNDERSTANDING Active Shape Models-Their Training and Application. *Computer Vision and Image Understanding*, *61*(1), 38–59.

Halmos, B., Tan, E. H., Soo, R. A., Cadranel, J., Lee, M. K., Foucher, P., Hsia, T. C., Hochmair, M., Griesinger, F., Hida, T., Kim, E., Melosky, B., Märten, A., & Carcereny, E. (2019). Impact of afatinib dose modification on safety and effectiveness in patients with EGFR mutation-positive advanced NSCLC: Results from a global real-world study (RealGiDo). *Lung Cancer*, *127*(October 2018), 103–111. https://doi.org/10.1016/j.lungcan.2018.10.028

Kustanto, Widodo, S., & Tomo. (2015). Software Development To Detect Lung Nodules in Computed Tomography Scan Image Using Support Vector Machine. *International Research Journal of Engineering and Technology (IRJET)*, *02*(06), 354–360. www.irjet.net

Makaju, S., Prasad, P. W. C., Alsadoon, A., Singh, A. K., & Elchouemi, A. (2018). Lung Cancer Detection using CT Scan Images. *Procedia Computer Science*, *125*(2009), 107–114. https://doi.org/10.1016/j.procs.2017.12.016

Onishi, Y., Teramoto, A., Tsujimoto, M., Tsukamoto, T., Saito, K., Toyama, H., Imaizumi, K., & Fujita, H. (2019). Automated Pulmonary Nodule Classification in Computed Tomography Images Using a Deep Convolutional Neural Network Trained by Generative

Vol. 10, No. 04; 2025

ISSN: 2456-3676

Adversarial Networks. *BioMed Research International*, *2019*(January). https://doi.org/10.1155/2019/6051939

Song, Q. Z., Zhao, L., Luo, X. K., & Dou, X. C. (2017). Using Deep Learning for Classification of Lung Nodules on Computed Tomography Images. *Journal of Healthcare Engineering*, *2017*. https://doi.org/10.1155/2017/8314740

Teramoto, A., Yamada, A., Kiriyama, Y., Tsukamoto, T., Yan, K., Zhang, L., Imaizumi, K., Saito, K., & Fujita, H. (2019). Automated classification of benign and malignant cells from lung cytological images using deep convolutional neural network. *Informatics in Medicine Unlocked*, *16*(July), 100205. https://doi.org/10.1016/j.imu.2019.100205

Thompson, J. C., Fan, R., Black, T., Yu, G. H., Savitch, S. L., Chien, A., Yee, S. S., Sen, M., Hwang, W. T., Katz, S. I., Feldman, M., Vachani, A., & Carpenter, E. L. (2019). Measurement and immunophenotyping of pleural fluid EpCAM-positive cells and clusters for the management of non-small cell lung cancer patients. *Lung Cancer*, *127*(November 2018), 25–33. https://doi.org/10.1016/j.lungcan.2018.11.020

Tian, Y., Shi, Y., & Liu, X. (2012). Recent advances on support vector machines research. *Technological and Economic Development of Economy*, *18*(1), 5–33. https://doi.org/10.3846/20294913.2012.661205

Tran, G. S., Nghiem, T. P., Nguyen, V. T., Luong, C. M., Burie, J. C., & Levin-Schwartz, Y. (2019). Improving Accuracy of Lung Nodule Classification Using Deep Learning with Focal Loss. *Journal of Healthcare Engineering*, *2019*. https://doi.org/10.1155/2019/5156416

Widodo, S., Rosyid, I., Faizuddin Bin Noor, M., & Bin Ismail, R. (2020). Texture Feature Extraction To Improve Accuracy of Malignant and Benign Cancer Detection on CT-Scan Images. *International Journal of Psychosocial Rehabilitation*, *24*(09), 3540–3554.

Zhou, T., Lu, H., Zhang, J., & Shi, H. (2016). Pulmonary nodule detection model based on SVM and CT image feature-level fusion with rough sets. *BioMed Research International*, *2016*. https://doi.org/10.1155/2016/8052436